https://dx.doi.org/10.1016/j.ymssp.2022.108901

Stiffness Identification of Magnetic Suspension System based on Zero-displacement and Zero-current Models

Biao Xiang[1], Zhongbo Li[1] and Waion Wong[2, *]

1, School of Mechano-Electronic Engineering, Xidian University,

Xi'an 710071, China

2, Department of Mechanical Engineering, The Hong Kong Polytechnic University, Kowloon,

Hong Kong SAR, China

Abstract—Based on the dynamic displacement and the control current of the magnetically suspended flywheel (MSFW) system with great self-weight, an identification method of the displacement and current stiffnesses of MSFW rotor is proposed in this article. The structure of MSFW rotor is introduced, and the dynamic displacement models of MSFW rotor in radial directions are established. Furthermore, to obtain the current stiffness and the displacement stiffness, control models including the zero-displacement model and the zero-current model are designed for MSFW rotor, and then the frequency characteristics of the zero-displacement model and the zero-current model are analyzed. Finally, experiments are conducted to measure the synchronous components of dynamic displacements and control currents so that the displacement and current stiffnesses of the MSFW system can be estimated.

Index Terms: magnetically suspended flywheel; stiffness estimation; zero-displacement model; zero-current model; dynamic displacement

1. Introduction

Active magnetic bearing (AMB) is commonly used to provide non-contact suspension for the levitation of the rotor of magnetically suspended flywheel (MSFW) system. In comparison to mechanical bearing, the AMB system has the advantages of active-controllability [1, 2], zero-friction [3, 4] and lubrication-free [5, 6]. Therefore, it had been used in high energy density motor [7, 8], centrifugal compressor [9], vacuum pump system [10-12], robot control system [13] and inertially stabilized platform [14]. Based on the basic model of magnetic force generated by the AMB system, the closed-loop control model could be designed for stable position control of the MSFW rotor suspended by the AMB system. The displacement stiffness and the current stiffness are the two most critical parameters for building up the force model of

AMB system. Therefore, an accurate estimation of the displacement stiffness and the current stiffness is very important for precise position control of the MSFW rotor.

In general, the accurate parameter models of the displacement stiffness and the current stiffness could be obtained by using the modelling method based on the equivalent magnetic circuit [15] and finite element modelling (FEM) [16-18] method. For example, based on the equivalent magnetic circuit modelling method, some critical parameters of a radial hybrid magnetic bearing including the bias flux density, area of magnetic pole and control current could be evaluated, and then the optimal model of radial hybrid magnetic bearing could be developed [15]. The 3D FEM method could be used to model a combination of permanent magnet bearing and eddy current damper with a conductive layer along the magnets of the stator or rotor, and a complete analytical method was performed to calculate the stiffness and rotating damping. The accuracy of analytical model was estimated quantitatively using 3D finite element analysis [16]. However, in the theoretical modelling of the magnetic bearing system including the equivalent magnetic circuit and the FEM, the displacement stiffness and the current stiffness are derived based on the ideal equivalent magnetic circuit and the FEM model. The reluctances and the magnetic flux leakage are neglected in the equivalent magnetic circuit modelling method. On the other hand, the subdivision grid of FEM model could not be infinity small. Therefore, there is obvious error between the theoretical predictions and the actual values of the displacement stiffness and the current stiffness. On the other hand, the parameter estimation method could also be used to identify the stiffness coefficients of magnetic bearing system [19-22]. A closed-loop system identification based on the genetic-algorithm weight least-mean-square (LMS) method was used to obtain the frequency-weight model of the AMB system, so the accurate modeling of AMB system was the key for a successful design of high-performance stable controller [19]. However, the cross-coupling effect at low frequency was not considered. Based on the Timoshenko beam rotor model, the unbalance response method was applied to identify the stiffness and damping of AMB system [20]. Although the stiffness and damping of rotor were estimated from 1200rpm to 30000rpm, the suspension force model of the AMB was not established. An identification algorithm based on LMS was used to estimate the force–displacement and the force–current coefficients of the AMB-rotor system with residual unbalances [23], and the estimated values of AMB were found to be in close range with that of theoretical values, but no experimental result at different rotational speeds was shown for verification of their theory.

In view of the above-mentioned problems, based on a zero-displacement model and a zero-current model, a stiffness identification method of magnetic suspension system making use of the MSFW rotor's residual unbalance and vibration is proposed. The synchronous components of rotor displacements and control currents at different rotational speeds are used to derive the displacement stiffness and the current stiffness of MSFW rotor. The proposed method has the advantage of no additional component and cost because it just makes use of the displacement sensor and the current sensor which are standard components of MSFW system. More importantly, this method is implementable by designing the zero-displacement and zero-current models, and the accuracy of the identified stiffness could be calibrated by choosing multiple sets of data about the synchronous components at different rotational speeds. The major contributions of this research work are listed below.

1. Control models including the zero-displacement model and the zero-current model are designed for MSFW rotor.
2. Frequency characteristics of MSFW rotor with the zero-displacement and the zero-current model are analyzed.
3. Synchronous components of dynamic displacements and control currents are used for the stiffness estimation.

This article is organized as follows. Section 1 is the introduction. In Section 2, the structure and dynamic models of MSFW rotor are introduced, and the model of stiffness estimation based on the dynamic displacement is established. The control model of MSFW rotor with the zero-displacement deflection model and the zero-current control model are designed in Section 3. The numerical simulations including the characteristics of the zero-displacement deflection model and the zero-current control model are conducted in Section 4. The experimental results are presented to verify the effectiveness of stiffness estimation method in Section 5. Finally, conclusions are drawn in Section 6.

2. Structure and Modeling of MSFW Rotor

2.1. *Modelling of MSFW Rotor*

The prototype of MSFW rotor is illustrated in Fig. 1(a). The two pairs of radial AMBs and the one pair of axial AMB in the magnetic suspension system provide magnetic forces to stably suspend the flywheel (FW) rotor at the equilibrium position in the radial and axial directions. The rotation of FW rotor about the axial principal axis is driven by the permanent magnet

synchronous motor (PMSM) of the MSFW system. The back-up ball bearing at the lower-end and the upper-end of the FW rotor is used to restrict the excessive displacement of FW rotor in case of the failure of magnetic suspension system at high rotational speeds.

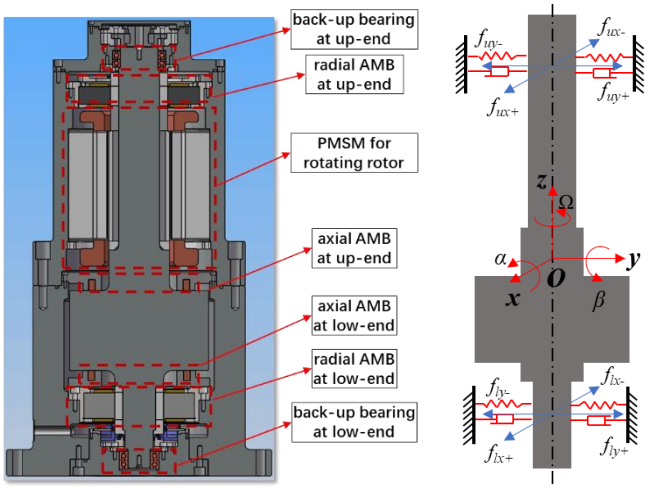

(a) (b)

Fig. 1. (a) The prototype of MSFW system, (b) the radial force model of MSFW rotor.

In the design of position control of the FW rotor with six degree-of-freedoms (DOFs), its rotational DOF about the z axis is controlled by the PMSM, and the translational DOFs along the z axis is controlled by the axial AMB. The two translational DOFs along the x and y axes are controlled by the radial AMBs, and the torque between the radial AMBs at the upper-end and the lower-end could control the tilting DOFs about the x and y axes. Fig. 1(b) shows the force model of MSFW rotor in radial direction. The equations of motion of the FW rotor are written as

$$\begin{aligned} m\ddot{x}_c &= f_{ux} + f_{lx} \\ m\ddot{y}_c &= f_{uy} + f_{ly} \\ J_x\ddot{\alpha} &= f_{uy}l - f_{ly}l + J_z\Omega\dot{\beta} \\ J_y\ddot{\beta} &= f_{ux}l - f_{lx}l - J_z\Omega\dot{\alpha} \end{aligned} \tag{1}$$

where J_x=J_y is the equatorial moment of inertia, and J_z is the polar moment of inertia. x_c and y_c are the displacement deflections of the geometric center of FW rotor along x and y axis, respectively. l is the suspension span of the radial AMBs. α and β are tilting angles of FW rotor about radial axes, respectively. Ω is the rotational speed of FW rotor about the axial principal axis.

2.2. *Magnetic Force of Radial AMB*

The stator of radial AMB is illustrated in Fig. 2(a). Eight groups of electrical windings in

the stator are connected to form two pairs of radial AMB. The red line in the figure is the path of magnetic flux generated by the stator windings in the four directions x+, y+, x- and y-. The equivalent magnetic circuits of radial AMB along the four directions are illustrated in Fig. 2(b). The magnetic fluxes pass through the stator core, the magnet ring, the airgap and the FW rotor. The equivalent reluctances of the airgap and the magnet ring are represented by R_1~R_8 as shown in Fig. 2(b), and they are in series connection within the same control channel.

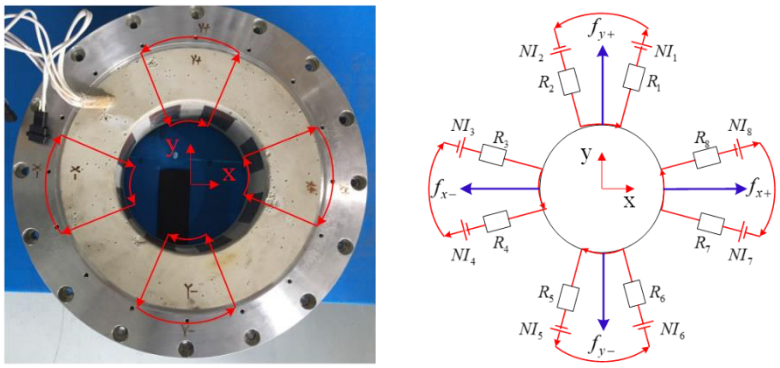

(a) (b)

Fig. 2. (a) The stator windings of radial AMB, (b) the equivalent magnetic circuit of radial AMB.

Considering the structural symmetry of the radial AMB, the magnetic force in x direction is chosen as the representative example in the following analysis. Based on the *Biot-savart*'s law, the magnetic forces of radial AMB in x direction of the four control channels could be written as

$$\begin{cases} f_{x-} = \dfrac{\Phi_{x-}^2}{\mu_0 A_{x-}} \\ f_{x+} = \dfrac{\Phi_{x+}^2}{\mu_0 A_{x+}} \end{cases} \tag{2}$$

The resultant magnetic force generated by the radial AMB in the x axis can be written as

$$f_x = f_{x+} - f_{x-} = \frac{\mu_0 A N^2}{4}\left[\frac{(I_0+i_x)^2}{(d_0-x_g)^2} - \frac{(I_0-i_x)^2}{(d_0+x_g)^2}\right] \tag{3}$$

where I_0 is the equivalent bias current. d_0 is the equivalent bias displacement, and i_x is the equivalent control current.

Within the vicinity of the radial equilibrium position, the derivative of magnetic force with respect to the control displacement is the displacement stiffness, and the derivative of magnetic force with respect to the control current is defined as the current stiffness. The current stiffness k_{ix} and the displacement stiffness k_{dx} could be written respectively as

$$\begin{cases} k_{ix} = k_{iy} = \frac{\mu_0 A N^2 I_0}{d_0^2} \\ k_{dx} = k_{iy} = -\frac{\mu_0 A N^2 I_0^2}{d_0^3} \end{cases} \tag{4}$$

Therefore, the respective magnetic forces of radial AMB along x and y directions are

$$\begin{cases} f_x = k_{ix} i_x + k_{dx} x_g \\ f_y = k_{iy} i_y + k_{dy} y_g \end{cases} \tag{5}$$

2.3. *The Dynamic Displacement Modelling of MSFW Rotor*

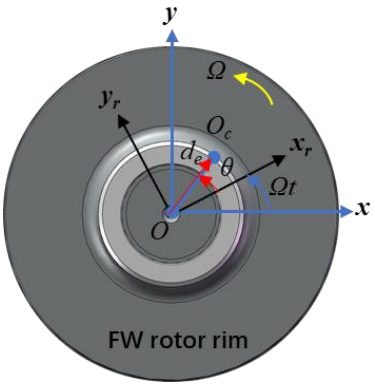

Fig. 3. The dynamic displacement diagram of MSFW rotor with unbalanced displacement terms.

When the FW rotor works at rotational speed Ω, the dynamic displacement of FW rotor with unbalanced displacement terms are shown in Fig. 3. The mass center of FW rotor is denoted as point $\boldsymbol{O_c}$ of coordinate (x_c, y_c), and the geometric center of FW rotor is denoted as point $\boldsymbol{O}$ of coordinate (x_g, y_g). The constant displacement deflection from the mass center $\boldsymbol{O_c}$ to the geometric center $\boldsymbol{O}$ is the unbalance displacement d_e. Furthermore, the fixed coordinate system of FW rotor is denoted as $\boldsymbol{Oxy}$, and the rotational coordinate system of FW rotor with the unbalance term is denoted as $\boldsymbol{Ox_ry_r}$. The angle between the unbalance displacement and the $\boldsymbol{x_r}$ axis of rotational coordinate is θ, and the angle between the fixed coordinate and the rotational coordinate is expressed as $\Omega \cdot t$ which varies in the time. Based on the fixed mass center of FW rotor, the dynamic displacement of geometric center could be expressed as

$$\begin{cases} x_c = x_g + d_e \cos(\Omega t + \theta) \\ y_c = y_g + d_e \sin(\Omega t + \theta) \end{cases} \tag{6}$$

The magnetic forces generated by the radial AMB is acting on the mass center $\boldsymbol{O_c}$ of FW rotor while the displacement deflections of geometric center $\boldsymbol{O}$ are measured by the displacement sensors.

Substituting the magnetic forces in Eq. (5) and the dynamic displacements in Eq. (6) into

the first two equations of Eq. (1), we have

$$\begin{cases} m\ddot{x}_g = k_{ix} i_x + k_{dx} x_g + m d_e \Omega^2 \cos(\Omega t + \theta) \\ m\ddot{y}_g = k_{iy} i_y + k_{dy} y_g + m d_e \Omega^2 \sin(\Omega t + \theta) \end{cases} \tag{7}$$

In the general position control of MSFW rotor, the zero-displacement deflection control of geometric center i.e. x_g=0 and y_g=0, is applied to ensure the FW rotor to be suspended stably at the equilibrium position. The control currents in radial control channels could be resolved as following

$$\begin{cases} i_x = -\frac{m d_e \Omega^2 \cos(\Omega t+\theta)}{k_{ix}} \\ i_y = -\frac{m d_e \Omega^2 \sin(\Omega t+\theta)}{k_{iy}} \end{cases} \Rightarrow \begin{matrix} \|i_x\| = -\frac{m d_e \Omega^2}{k_{ix}} \\ \|i_y\| = -\frac{m d_e \Omega^2}{k_{iy}} \end{matrix} \tag{8}$$

Applying the zero-displacement control, the control current amplitudes are proportional to the square value of respective rotational speed.

Moreover, the zero-current model (i_x=0, i_y=0) of radial AMB is applied to the MSFW system, the displacement deflection of geometric center in Eq.(7) could be rewritten as

$$\begin{cases} x_g = -\frac{m d_e \Omega^2 \cos(\Omega t+\theta)}{k_{dx}+m\Omega^2} \\ y_g = -\frac{m d_e \Omega^2 \sin(\Omega t+\theta)}{k_{dy}+m\Omega^2} \end{cases} \Rightarrow \begin{matrix} \|x_g\| = -\frac{m d_e \Omega^2}{k_{dx}+m\Omega^2} \\ \|y_g\| = -\frac{m d_e \Omega^2}{k_{dy}+m\Omega^2} \end{matrix} \tag{9}$$

Eq.(9) shows that the displacement deflection amplitudes would be intensified by increasing the rotational speed.

Combing the amplitude parts of Eq.(8) and (9), we have

$$\begin{cases} k_{ix}\|i_x\| - k_{dx}\|x_g\| = m\|x_g\|\Omega^2 \\ k_{iy}\|i_y\| - k_{dy}\|y_g\| = m\|y_g\|\Omega^2 \end{cases} \tag{10}$$

Therefore, when the rotational speed is chosen as different values as this matrix [Ω_1 Ω_2 Ω_3 … Ω_n], and the zero-displacement and the zero-current control modes are applied to the MSFW system. At the corresponding rotational speed of MSFW system, the synchronous components of dynamic displacements in radial direction could be expressed as [x_{g1} x_{g2} x_{g3}… x_{gn}] and [y_{g1} y_{g2} y_{g3}… y_{gn}], and the synchronous components of control currents are [i_{x1} i_{x2} i_{x3}… i_{xn}] and [i_{y1} i_{y2} i_{y3}… i_{yn}]. Furthermore, Eq.(10) could be written in matrix form as following

$$\begin{bmatrix} \|i_x^n\| & \|x_g^n\| \\ \|i_x^{n+1}\| & \|x_g^{n+1}\| \end{bmatrix} \begin{bmatrix} k_{ix} \\ k_{dx} \end{bmatrix} = \begin{bmatrix} m\|x_g^n\|\Omega_1^2 \\ m\|x_g^{n+1}\|\Omega_2^2 \end{bmatrix} \Rightarrow \begin{bmatrix} k_{ix} \\ k_{dx} \end{bmatrix} = \begin{bmatrix} \|i_x^n\| & \|x_g^n\| \\ \|i_x^{n+1}\| & \|x_g^{n+1}\| \end{bmatrix}^{-1} \begin{bmatrix} m\|x_g^n\|\Omega_1^2 \\ m\|x_g^{n+1}\|\Omega_2^2 \end{bmatrix}$$

(11)

$$\begin{bmatrix} \|i_y^n\| & \|y_g^n\| \\ \|i_y^{n+1}\| & \|y_g^{n+1}\| \end{bmatrix} \begin{bmatrix} k_{iy} \\ k_{dy} \end{bmatrix} = \begin{bmatrix} m\|y_g^n\|\Omega_1^2 \\ m\|y_g^{n+1}\|\Omega_2^2 \end{bmatrix} \Rightarrow \begin{bmatrix} k_{iy} \\ k_{dy} \end{bmatrix} = \begin{bmatrix} \|i_y^n\| & \|y_g^n\| \\ \|i_y^{n+1}\| & \|y_g^{n+1}\| \end{bmatrix}^{-1} \begin{bmatrix} m\|y_g^n\|\Omega_1^2 \\ m\|y_g^{n+1}\|\Omega_2^2 \end{bmatrix} \tag{12}$$

Finally, by measuring the dynamic displacement deflections and the control currents of MSFW system at different rotational speed, the displacement stiffness and the current stiffness of radial AMB can be determined by using Eqs. (13) and (14) above.

3. The Control Model of MSFW Rotor

3.1. *The Close-loop Control Model of MSFW Rotor*

The zero-displacement model and the zero-current model are the major techniques to collect the synchronous components of control currents and displacement deflections when the MSFW system is operating at different rotational speeds. The control diagram of MSFW system in single control channel is shown in Fig. 4. N(s) is the notch filter to realize the zero-displacement model and the zero-current model. G_c(s) is the control model to realize the stable control of MSFW rotor. G_w(s) is the amplification unit to transfer the control voltage to the control current. G_p(s) in the red box is the equivalent control model of MSFW rotor, and k_s is the sensitivity of displacement sensor.

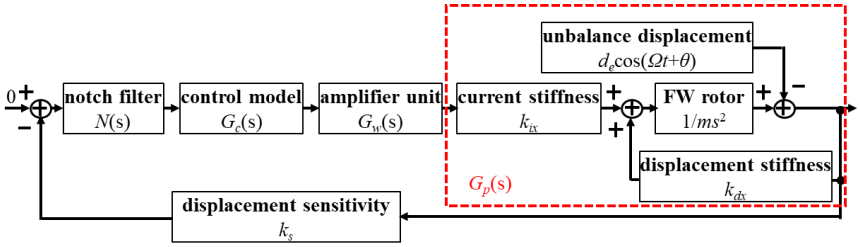

Fig. 4. The block diagram of control model with single control channel.

An incomplete differential PID model with time constant τ_f is designed for the control model G_c(s) as follows.

$$G_c(s) = K_P + \frac{K_I}{s} + \frac{K_D \tau_f s}{\tau_f s + 1} \tag{13}$$

The transfer function of amplification unit G_w(s) with time constant τ_w is expressed as

$$G_w(s) = \frac{k_w}{\tau_w s + 1} \tag{14}$$

The transfer function of control plant G_p(s) is expressed as

$$G_p(s) = \frac{k_{ix}}{ms^2 + k_{dx}} \tag{15}$$

3.2. *The Zero-Displacement Model of MSFW Rotor*

The control model of notch filter $N_{zero\text{-}dis}(s)$ in time-domain is designed for zero-displacement control of MSFW rotor in Fig. 5. $N_f(s)$ is the frequency selector, and ε is the coefficient of notch filter. $\boldsymbol{T}$ is the transformation matrix (T-matrix) with real parameters. $x(t)$ is the input signal. $y(t)$ is the output signal through the notch filter, and $e(t)$ is the error signal.

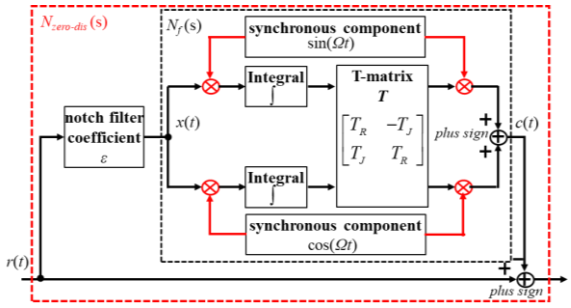

Fig. 5. The zero-displacement control model.

The output signal of filter with the synchronous components could be expressed as

$$\begin{aligned} c(t) = {} & [T_R \sin(\Omega t) + T_J \cos(\Omega t)] \int x(t) \sin(\Omega t) dt \\ & + [T_R \cos(\Omega t) - T_J sin(\Omega t)] \int x(t) cos(\Omega t) dt \end{aligned} \tag{16}$$

Given that $\dot{\Omega} = 0$, the derivative equation of Eq.(16) could be expressed as

$$\frac{d^2 c(t)}{dt^2} + \Omega^2 c(t) = T_R \frac{dx(t)}{dt} - T_J \Omega x(t) \tag{17}$$

Taking Laplace transformation of Eq. (19), we have

$$c(s)s^2 + \Omega^2 c(s) = T_R x(s)s - T_J \Omega x(s) \tag{18}$$

Furthermore, the frequency selector $N_f(s)$ could be obtained as follows.

$$N_f(s) = \frac{c(s)}{x(s)} = \frac{T_R s - T_J \Omega}{s^2 + \Omega^2} \tag{19}$$

The notch filter in the zero-displacement model is therefore designed as

$$N_{zero-dis}(s) = \frac{s^2 - \varepsilon T_R s + \Omega^2 + \varepsilon T_J \Omega}{s^2 + \Omega^2} \tag{20}$$

The amplitude-frequency functions could be expressed as

$$\|N_{zero-dis}(\omega)\| = \frac{\sqrt{\left(\Omega^2 + \varepsilon T_J \Omega - \omega^2\right)^2 + (\varepsilon T_R \omega)^2}}{|\Omega^2 - \omega^2|} \tag{21}$$

The frequency bandwidth $\Delta\omega$ of notch filter is introduced and written as

$$\begin{cases} \|N_{zero-dis}(\omega)\|\|_{\omega=\Omega} = \infty \\ \|N_{zero-dis}(\omega)\|\|_{\substack{\omega-\Delta\omega\to\Omega \\ \omega+\Delta\omega\to\Omega}} \approx \infty \end{cases} \tag{22}$$

Within the bandwidth of notch filter, the gain of notch filter would become infinite at the synchronous frequency of the rotor with rotational speed Ω, so the synchronous components of control currents would be obtained when the closed-loop control system is stable. Therefore, the zero-displacement control of MSFW rotor would be realized.

3.3. *The Zero-Current Model of MSFW Rotor*

Fig. 6 shows the zero-current control model of MSFW rotor with the same frequency selector structure of zero-displacement control model. The notch filter designed for zero-current control model could be expressed as

$$N_{zero-cur}(s) = \frac{s^2+\Omega^2}{s^2+\varepsilon T_R s+\Omega^2-\varepsilon T_J \Omega} \tag{23}$$

The amplitude-frequency functions could be expressed as

$$\|N_{zero-cur}(\omega)\| = \frac{|\Omega^2-\omega^2|}{\sqrt{\left(\Omega^2-\varepsilon T_J\Omega-\omega^2\right)^2+(\varepsilon T_R\omega)^2}} \tag{24}$$

Within the frequency bandwidth of rotational speed, the gain of notch filter could be expressed as

$$\begin{cases} \|N_{zero-cur}(\omega)\|\|_{\omega=\Omega} = 0 \\ \|N_{zero-cur}(\omega)\|\|_{\substack{\omega-\Delta\omega\to\Omega \\ \omega+\Delta\omega\to\Omega}} \approx 0 \end{cases} \tag{25}$$

Within the frequency bandwidth of notch filter, the gain of notch filter would be zero at the synchronous frequency of FW rotor with rotational speed Ω, so the synchronous components of control current would become zero when the closed-loop control system is stable. Therefore, the zero-current control of MSFW rotor would be accomplished.

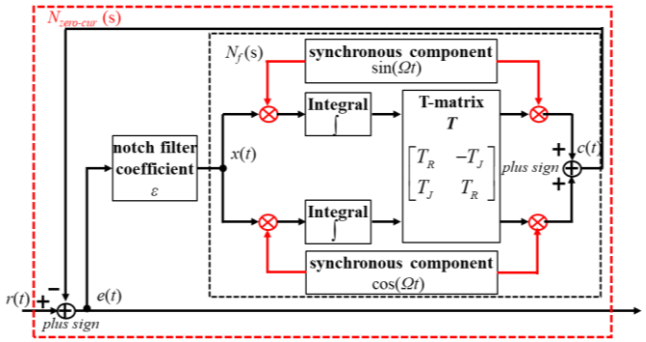

Fig. 6. The zero-current control model.

3.4. *The Stability Analysis of Closed-loop Control Model*

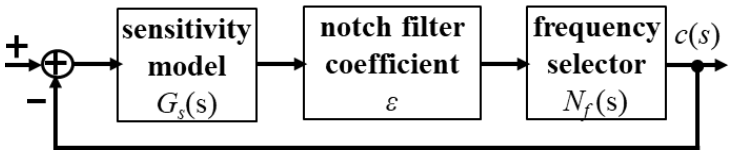

Fig. 7. The equivalent diagram of closed control loop with the notch filter.

The stability of the control system is the precondition of applying the above-mentioned two control modes. The sensitivity model G_s(s) in Fig. 7 is therefore introduced to design the T-matrix to ensure the system stability. The sensitivity function of zero-displacement control model could be designed as a constant value term while the sensitivity function of zero-current control model is designed as follows.

$$G_s(s) = \frac{1}{1+N_f(s)} = \frac{s^2+\Omega^2}{s^2+T_R s+\Omega^2-T_J\Omega} \tag{26}$$

By defining the coefficient of T-matrix T_R with positive real number, the poles of sensitivity function in Eq. (26) has negative real parts.

The equivalent transfer function of closed-loop system with the notch filter in Fig. 7 is written as

$$G_n(s) = \frac{G_s(s)\varepsilon N_f(s)}{1+G_s(s)\varepsilon N_f(s)} \tag{27}$$

Substituting Eq.(19) into Eq.(27), we have

$$G_n(s) = \frac{(T_R s-T_J\Omega)\varepsilon G_s(s)}{s^2+\Omega^2+(T_R s-T_J\Omega)\varepsilon G_s(s)} \tag{28}$$

Using Eq. (30), the eigenvalue equation could be written as

$$eigen(s) = s^2 + \varepsilon T_R G_s(s)s - \varepsilon T_J\Omega G_s(s) + \Omega^2 = 0 \tag{29}$$

The partial derivative function of eigenvalue equation with respect to the coefficient ε could be expressed as

$$\frac{\partial eigen(s)}{\partial \varepsilon} = 2s\frac{\partial s}{\partial \varepsilon} + \varepsilon T_R G_s(s)\frac{\partial s}{\partial \varepsilon} + T_R G_s(s)s - T_J\Omega G_s(s) = 0 \tag{30}$$

Assuming the coefficient ε=0 and the eigenvalue $s=j\Omega$, Eq.(30) could be rewritten as

$$\left.\frac{\partial s}{\partial \varepsilon}\right|_{\substack{\varepsilon=0 \\ s=j\Omega}} = -\frac{1}{2}(T_R + jT_J)G_s(j\Omega) \tag{31}$$

If the real part of Eq.(31) could satisfy the following condition

$$Re\left(\left.\frac{\partial s}{\partial \varepsilon}\right|_{\substack{\varepsilon=0 \\ s=j\Omega}}\right) \le 0 \tag{32}$$

The locus of the eigenvalues could be located on the left half plane when the coefficient of the notch filter $\varepsilon > 0$, so the stability of closed-loop control system can be guaranteed. Therefore,

the coefficients of T-matrix could be chosen as $T_R + j\ T_J = G_s(j\Omega)^{-1}$, where T_R is the real part, and T_j is the imaginary part.

4. Numerical Simulation

4.1. *The Frequency Characteristics of Zero-displacement Model*

The coefficient ε is 1, and the coefficients of T-matrix are $T_R = 1$ and $T_J = 0$. The frequency response diagrams of notch filter with the center frequency in the zero-displacement control model is chosen as 33.33Hz (2000rpm), 66.66Hz (4000rpm), 1000Hz (6000rpm) and 133.33Hz (8000rpm), respectively, are measured and plotted in Fig. 8(a). At the center frequency, the amplitude of notch filter is infinite, and the synchronous components of control currents could be obtained when the closed-loop control system is stable. Therefore, the zero-displacement deflection control of MSFW rotor would be realized.

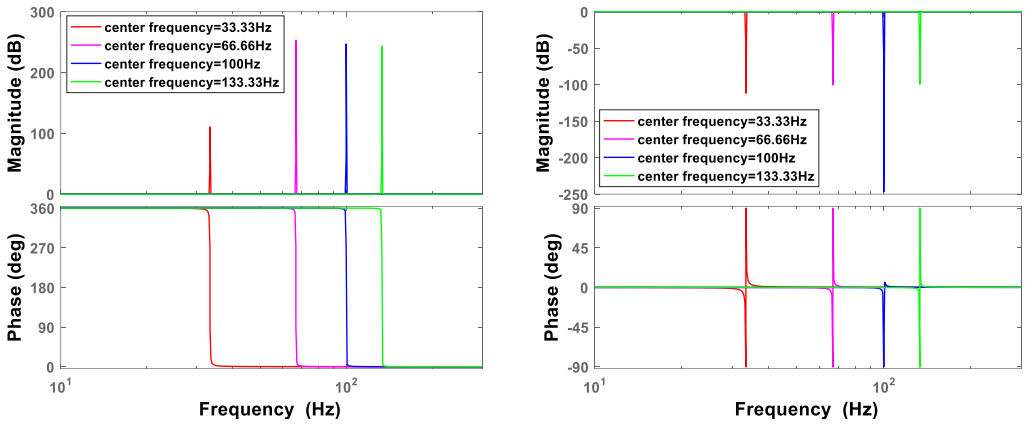

Fig. 8. The frequency responses of notch filter in the zero-displacement control model, (b) the frequency responses of notch filter in the zero-current control model.

4.2. *The Frequency Characteristics of Zero-Current Model*

The frequency response diagrams of notch filter in the zero-current control model are illustrated in Fig. 8(b). The response amplitude of notch filter is practically zero at the center frequency. Moreover, the synchronous components of control current are practically zero when the closed-loop control system is stable. Therefore, the zero-current control of MSFW rotor would be accomplished.

4.3. *The Stability Estimation of Closed-loop Control Model*

By choosing the parameters in the Section 4.1, the sensitivity function $G_s(s)$ of zero-current

control model could be written as

$$G_s(s) = \frac{1}{1+N_f(s)} = \frac{s^2+\Omega^2}{s^2+s+\Omega^2} \tag{33}$$

For the closed-loop control system with the zero-displacement control model, the root locus of transfer function is plotted in Fig. 9(a) with the rotational speed of MSFW rotor chosen respectively as 33.33Hz (2000rpm), 66.66Hz (4000rpm), 1000Hz (6000rpm) and 133.33Hz (8000rpm). The real parts of the closed-loop system are all located on the left half plane (LHP). Therefore, the closed-loop control system with the zero-displacement deflection control model is stable. For the closed-loop control system with the zero-current control model, the root loci of the transfer function at different rotational speeds are illustrated in Fig. 9(b), and all the roots of closed-loop transfer function are located on the LHP. Therefore, based on the chosen parameters of notch filter coefficient and T-matrix in the Section 4.1, the closed-loop control system of MSFW system in Fig. 4 is stable.

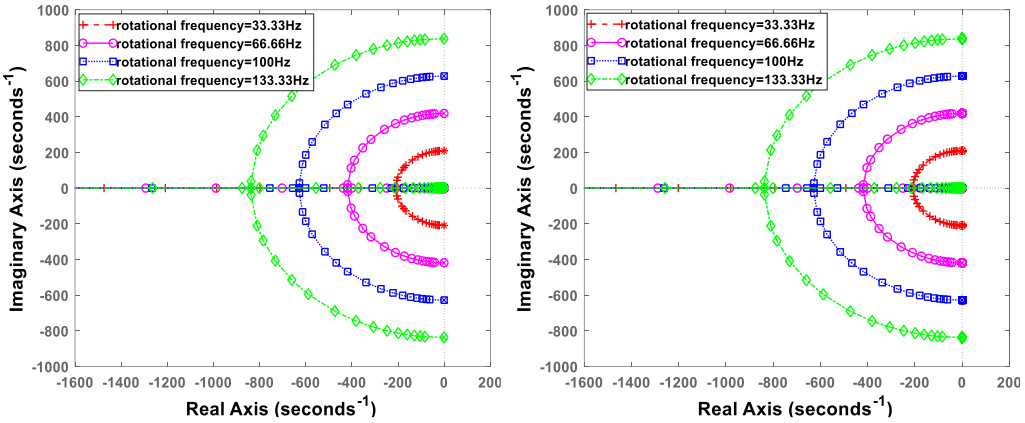

(a) (b)

Fig. 9. (a) The root locus of the closed-loop transfer function with zero-displacement control model, (b) the root locus of the closed-loop transfer function with zero-current control model.

5. Experiment

5.1. *Experimental Setup*

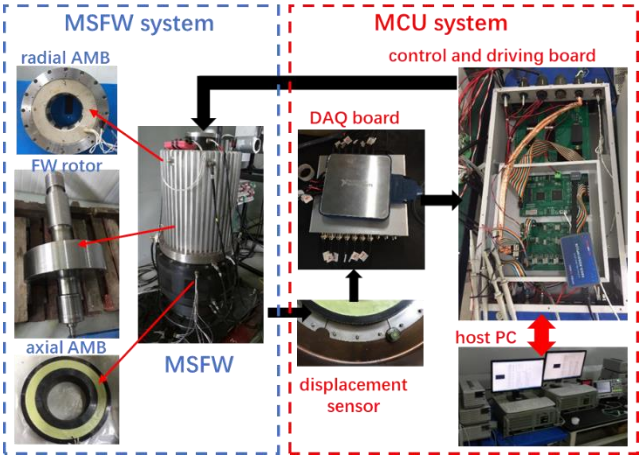

Fig. 10. The whole system of the MSFW rotor.

The experiment setup of whole MFSW system is shown in Fig. 10. It consists of the mechanical part of MFSW system and the main control unit (MCU). The mechanical part of MSFW system has two pairs of radial AMBs, one pair of axial AMBs, a FW rotor and a PMSM. The power supply system has an output voltage of 28V and current of 2A is used to drive the axial and radial AMBs. The vacuum pump is used to provide the vacuum condition in MSFW system, and it also reduce the wind drag when the MSFW rotor works at a high speed. In the MCU of MSFW system, the eddy current displacement sensors are used to measure displacement deflections of MSFW rotor from its equilibrium position. The data acquisition (DAQ) board NI PCI 6355 could timely collect and feedback the displacement deflections of FW rotor to the MCU mainly based on a digital signal processor (DSP) chip TMS320F28335 and a field programmable gate array (FPGA) chip Altera EPF10K30RC208. The host computer timely monitors operation statuses of experimental setup such as the rotational speed, the degree of vacuum, the control currents and the dynamic displacement deflections. The major parameters and their respective values of MSFW system are listed in TABLE. I.

Furthermore, according to the numerical simulation, the stabilities of zero-current and zero-displacement control models are guaranteed. Therefore, the experiments about MSFW rotor with zero-current and zero-displacement control models are carried out. Moreover, the displacement variations and control currents of MSFW rotor are measured to identify the stiffness characteristics of MSFW system.

TABLE. I. THE PARAMETERS OF THE MSFW SYSTEM.

Symbol	Definition	Value	Symbol	Definition	Value
k_{dx}	nominal displacement stiffness	-1700 N/mm	J_x, J_y	equatorial moment of inertia	1.24 kg·m^2
k_{ix}	nominal current stiffness	620 N/A	J_z	polar moment of inertia	0.67 kg·m^2
m	mass of FW rotor	150 kg	l	suspension span	0.48 mm

k_s	displacement sensitivity	3.3V/mm	k_w	power amplifier	0.2A/V
K_I	integral coefficient	0.0075	K_P	proportional coefficient	6.15
τ_w	time constant of amplifier	$5\cdot10^{-5}$s	K_D	derivative coefficient	21
Ω	rotational speed	2000/4000 /6000/8000 rpm	τ_f	time constant of incomplete derivate PID	$2\cdot10^{-3}$s

5.2. *The Process of Stiffness Estimation based on Dynamic Displacement*

The identification process of both displacement and current stiffnesses based on the dynamic displacement measurement are presented in Fig. 11, and steps of identification process are listed in the following.

1. After initializing the parameters of the MSFW system and setting the reference rotational speed, the zero-displacement deflection control model is loaded.
2. The control current of the MSFW system could then be collected and recorded by the host PC and the oscilloscope when the MSFW system could be stably suspended at the equilibrium position.
3. Furthermore, the rotational speed of the MSFW system is slowed down to the static state, and then the zero-current control program is loaded. The displacement deflections of the MSFW rotor from the equilibrium position could then be recorded.
4. Finally, the dynamic displacement deflections and the control currents could be substituted to the solution equations of Eqs. (11) and (12) for the determination of the current stiffness and the displacement stiffness of the MSFW system.

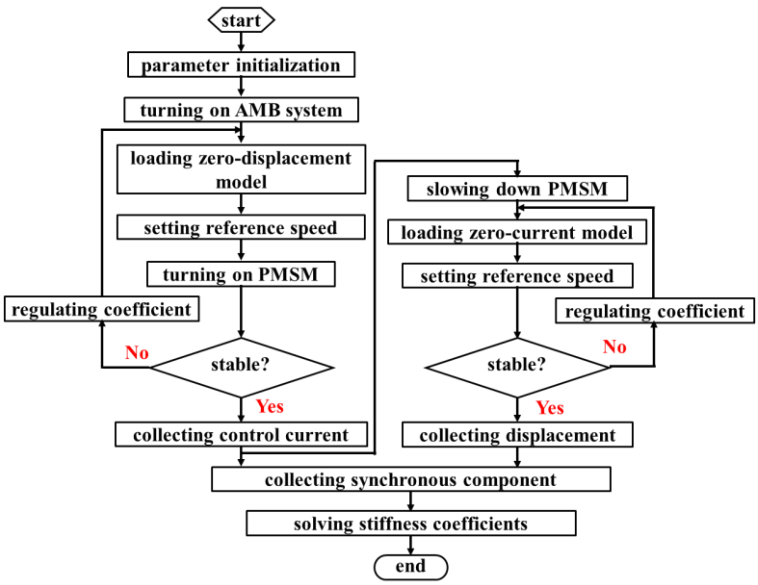

Fig. 11. The flowchart of stiffness estimation based on the dynamic displacement measurement.

5.3. *The Suspension Performance of MSFW System*

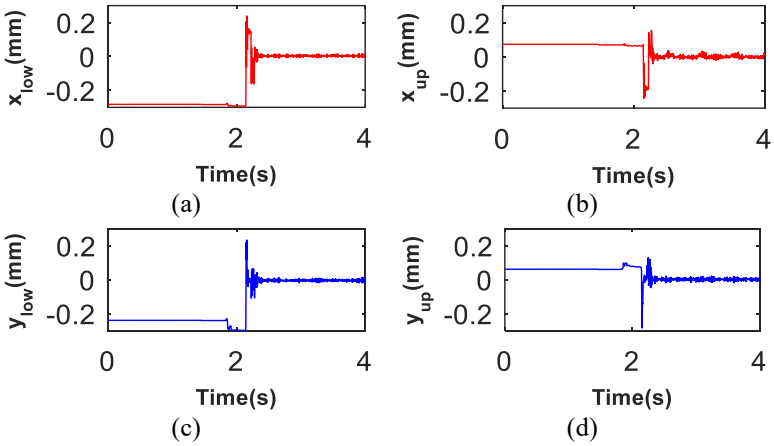

Fig. 12. The suspension trace of MSFW rotor, (a) the dynamic displacement at the lower-end along *x* axis, (b) the dynamic displacement at the upper-end along *x* axis, (c) the dynamic displacement at the lower-end along *y* axis, (d) the dynamic displacement at the upper-end along *y* axis.

Firstly, a step signal is used as the reference input to suspend MSFW rotor at the equilibrium position in radial direction, and the suspension traces of MSFW rotor at the lower-end and the upper-end in radial direction are shown in Fig. 12. The displacement deflections of MSFW rotor at the upper-end and the lower-end are at the initial value when there is no magnetic force acting on the MSFW rotor, and then the displacement deflection of MSFW rotor is equal to zero when the magnetic forces are imposed on the MSFW rotor, so the MSFW rotor is suspended at the equilibrium position in radial direction. Therefore, the suspension test of MSFW rotor could verify that the magnetic forces generated by the magnetic suspension system could stably suspend the MSFW rotor.

5.4. *The Dynamic Displacements of MSFW System with Zero-current Model*

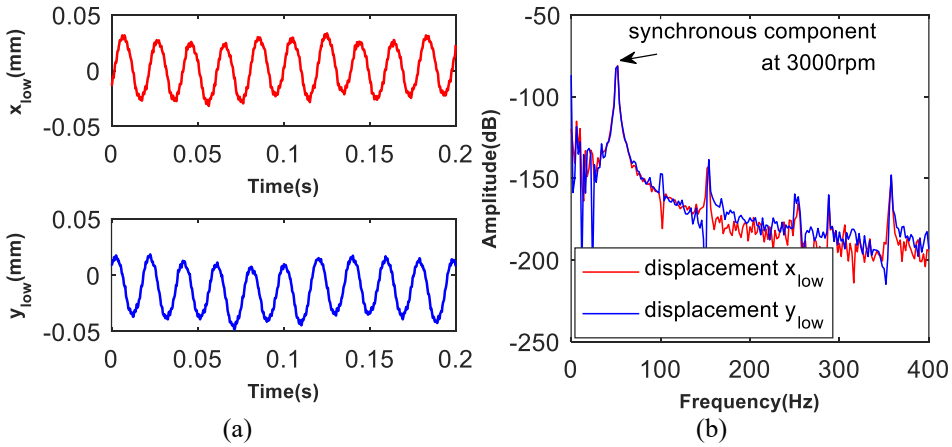

Fig. 13. The dynamic displacements of MSFW rotor at 3000rpm, (a) dynamic displacements at lower-end of the MSFW rotor, (b) the power spectra of dynamic displacements.

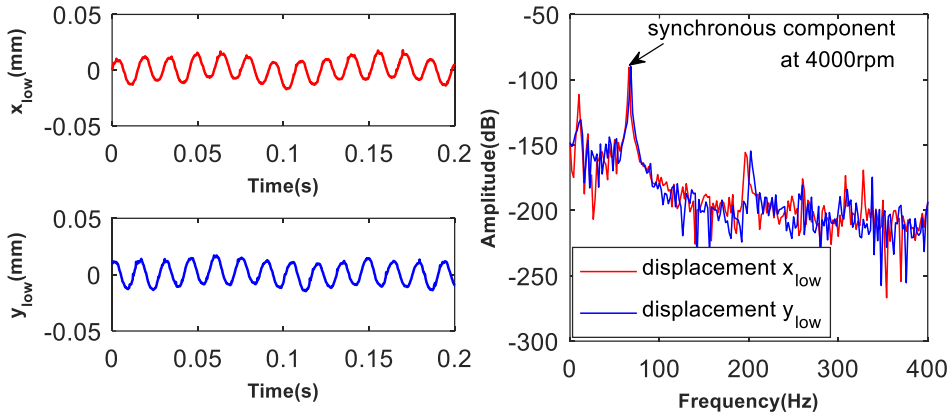

(a) (b)

Fig. 14. The dynamic displacements of MSFW rotor at 4000 rpm, (a) dynamic displacements at lower-end of the MSFW rotor, (b) the power spectra of dynamic displacements.

In this section, the displacement deflections of MSFW rotor with the zero-current model are measured, and the displacement deflections at the lower-end of the MSFW rotor are chosen as the analysis case considering the structure symmetry of MSFW rotor. When the rotational speed of MSFW rotor is at 3000rpm, the displacement deflections at the lower-end of FW rotor are shown in Fig. 13(a). The power spectra of dynamic displacements are plotted in Fig. 13(b) to collect the synchronous components of dynamic displacements at 3000rpm. As shown in Fig. 13(b), the synchronous component of dynamic displacement at 3000rpm (50Hz) is about 21μm. Similarly, the dynamic displacements of MSFW rotor at 4000rpm (about 66.67Hz) are plotted in Fig. 14, and the synchronous component of dynamic displacement at 4000rpm is about 16μm.

5.5. *The Control Currents of MSFW System with Zero-displacement Model*

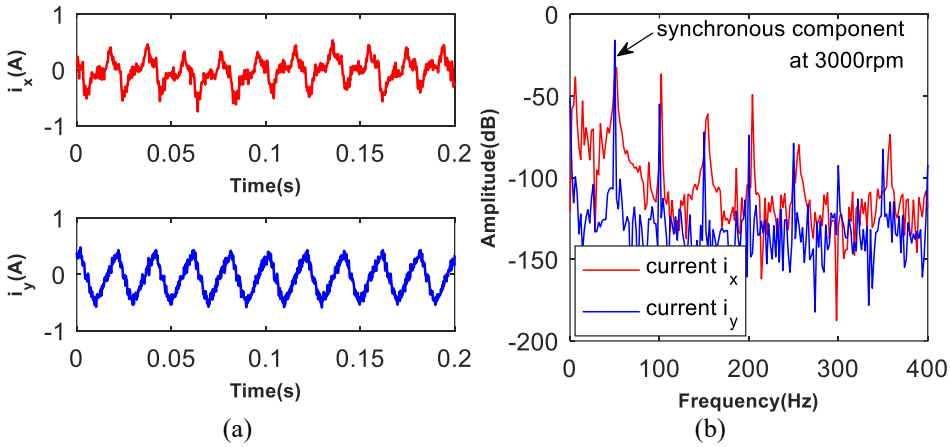

(a) (b)

Fig. 15. The control currents of MSFW system at 3000 rpm, (a) the control currents of radial AMB at lower-end of the MSFW rotor, (b) the power spectra of control currents.

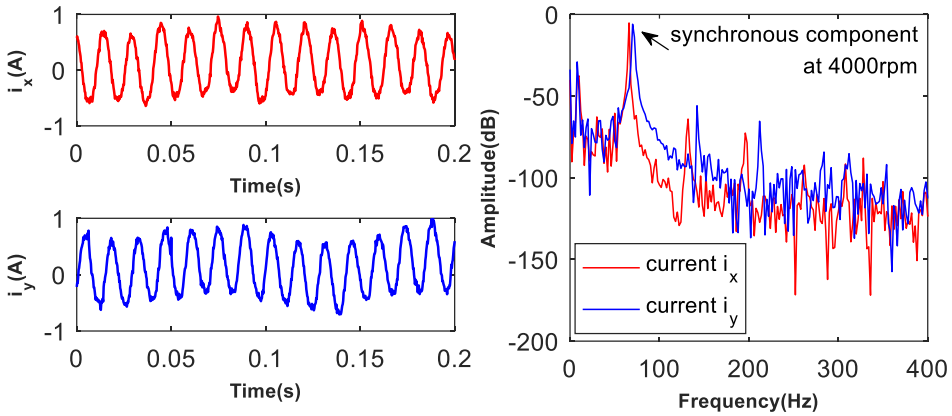

(a) (b)

Fig. 16. The control currents of MSFW system at 4000 rpm, (a) the control currents of radial AMB at lower-end of the MSFW rotor, (b) the power spectra of control currents.

Moreover, the control currents of MSFW rotor with the zero-displacement model are recorded, and the control currents of MSFW system at the lower-end are analyzed. The control currents with the MSFW rotor running at 3000rpm are recorded and plotted in Fig. 15. The control current i_x is displayed by the red line while the control current i_y is shown by the blue line. As illustrated in Fig. 15(b), the control current of the MSFW system at 3000rpm is found to be 0.55A. When the rotational speed of MSFW rotor is 4000rpm, the control currents of MSFW rotor are recorded and plotted in Fig. 16. The synchronous component of control currents is found to be 0.72A.

5.6. *The Stiffness Solution of MSFW System*

The synchronous components of dynamic displacements are recorded at speeds from 2000 rpm to 6000 rpm and they are marked and plotted as the blue line in Fig. 17(a). The synchronous displacement of MSFW rotor decreases with the increase of rotational speed because of the self-centering effect. Moreover, the synchronous components of control currents are also recorded and plotted as the red line in Fig. 17(a). The synchronous current of MSFW system is increased when the rotational speed is accelerated from 2000 rpm to 6000 rpm to suppress the displacement deflection of MSFW rotor. Moreover, the unbalance vibration forces of MSFW rotor from 2000rpm to 6000rpm are determined using Eq. (10) and plotted Fig. 17(b). It can be seen in Fig. 17(b) that the unbalance vibration forces are intensified with the increase of rotational speed.

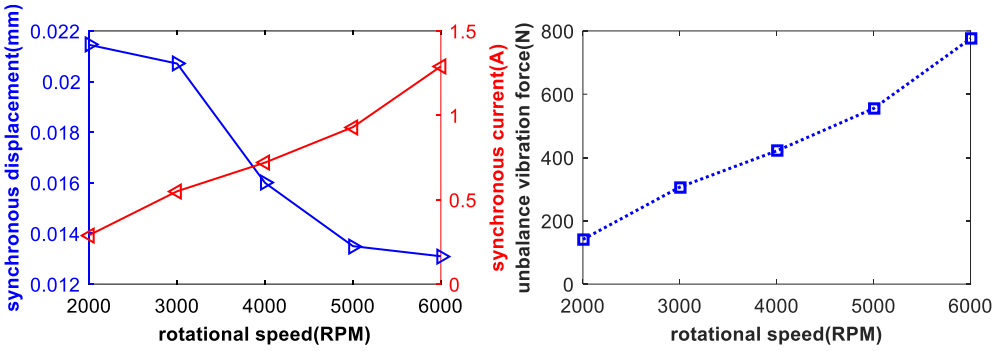

(a) (b)

Fig. 17. (a) The synchronous displacements and currents of MSFW rotor at different rotational speeds, (b) the unbalance vibration force of MSFW rotor at different speeds.

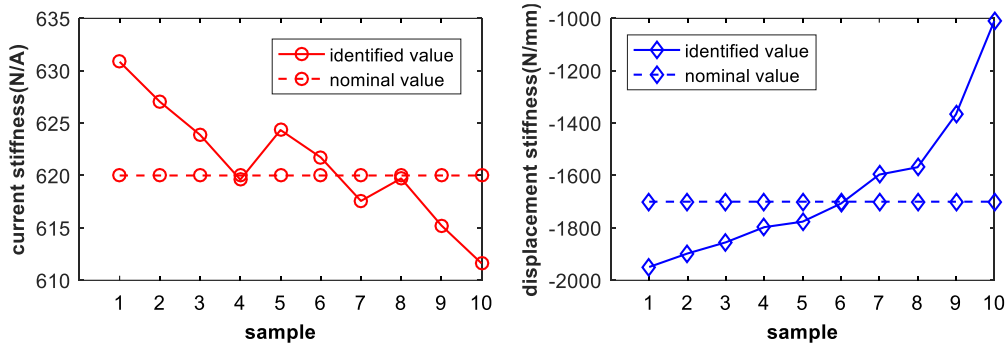

(a) (b)

Fig. 18. (a) The current stiffness obtained by the dynamic displacements and the control currents, (b) the displacement stiffness obtained by the dynamic displacements and the control currents.

Based on the synchronous components of dynamic displacements with the zero-current and the control currents with the zero-displacement model, the displacement stiffness and current stiffness could be determined based on Eq. (11). Furthermore, substituting synchronous displacements, synchronous currents and unbalance vibration forces into Eq. (11), we have

$$\begin{bmatrix} i_{x1} & x_1 \\ i_{x2} & x_2 \end{bmatrix} \begin{bmatrix} k_{ix} \\ k_{dx} \end{bmatrix} = \begin{bmatrix} m\Omega_1^2 x_1 \\ m\Omega_2^2 x_2 \end{bmatrix} \Rightarrow \begin{bmatrix} k_{ix} \\ k_{dx} \end{bmatrix} = \begin{bmatrix} i_{x1} & x_1 \\ i_{x2} & x_2 \end{bmatrix}^{-1} \begin{bmatrix} m\Omega_1^2 x_1 \\ m\Omega_2^2 x_2 \end{bmatrix} \tag{34}$$

By selecting two different groups of synchronous displacements, synchronous currents and unbalance vibration forces in Fig. 17, there are 10 combination sets as listed in Table II. The current stiffness and displacement stiffness obtained from Eq. (34) are plotted in Fig. 18(a) and 18(b), respectively. At the initial rotational speed of MSFW rotor, the suspension displacements of MSFW rotor obviously deflect from the center position so that the magnetic force of AMB deviate from the linear range, and a large control current is needed to force the MSFW rotor back to the center position. It can be observed in both Figs. 18(a) and 18(b) that there are large differences between the nominal value and the measured value of both the current and displacement stiffnesses. The large errors also occurred at high rotational speed because the unbalance vibration force is intensified.

TABLE. II. THE STIFFNESS ERRORS COMPARED TO THE NOMINAL VALUES.

set	current stiffness		displacement stiffness	
	error(N/A)	relative error(%)	error(N/mm)	relative error(%)
1 (2000+300 rpm)	10.85	1.72	249.26	12.79
2 (2000+4000rpm)	7.04	1.12	197.67	10.42
3 (2000+5000rpm)	3.88	0.62	154.99	8.36
4 (2000+6000rpm)	0.39	0.06	97.25	5.41
5 (3000+4000rpm)	4.34	0.69	76.28	4.29
6 (3000+5000rpm)	1.73	0.28	7.06	0.41
7 (3000+6000rpm)	2.43	0.39	103.46	6.48
8 (4000+5000rpm)	0.28	0.05	131.57	8.39
9 (4000+6000rpm)	4.76	0.77	333.33	24.39
10 (5000+6000rpm)	8.38	1.37	689.84	68.29

The absolute and percentage errors of stiffnesses are listed in TABLE. II. The maximum error of current stiffness is about 10.85 N/A or 1.72% relative error occurring at the set of 2000 rpm and 3000 rpm, and the minimum error is about 0.28 N/A or 0.05% relative error at the set of 4000 rpm and 5000 rpm. For the displacement stiffness, the maximum error is about 689.84 N/mm or 68.29% relative error found in the set of 5000 rpm and 6000 rpm, and the minimum error is about 7.06 N/mm or 0.41% relative error found in the set of 3000 rpm and 5000 rpm. As shown in Fig. 19, the set 6 which is the group of 3000 rpm and 5000 rpm is chosen as the analysis sample, and the relative error of current stiffness in Fig. 19(a) is just about 0.28% while that of displacement stiffness in Fig. 19(b) is about 0.41%. The set 6 is therefore the best combination of estimated results.

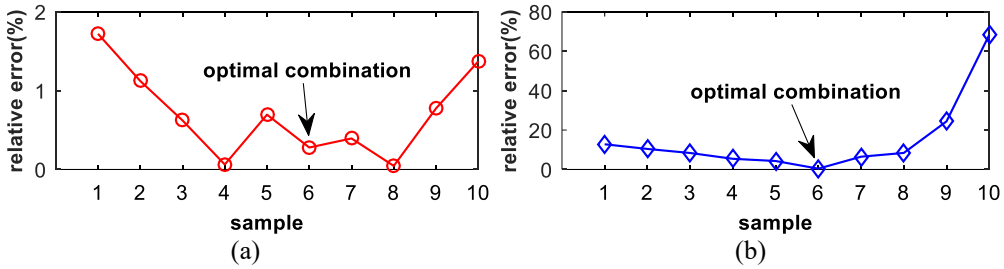

Fig. 19. The relative error between the nominal value and the identified value, (a) the relative error of current stiffness, (b) the relative error of displacement stiffness.

Overall, the stiffness estimation method based on the synchronous displacements and the

synchronous currents is proved to be useful to obtain the approximate stiffness coefficients of MSFW system when the speed combination is chosen wisely. However, a large estimation error would occur when the MSFW rotor rotates at the high rotational speed. The detailed reasoning of this phenomenon could be expressed by the flowchart in Fig. 20. The increasement of rotational speed and rotor mass could intensify the unbalance vibration of MSFW rotor, and the AMB system needs a greater control current to achieve zero-displacement control, so the error between the estimated value and the nominal value would be enlarged.

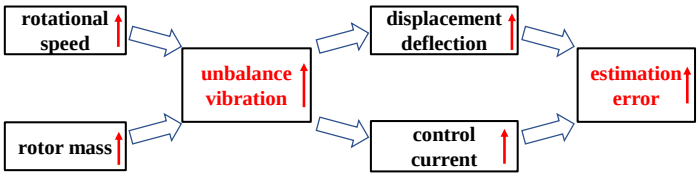

Fig. 20. The flowchart of estimation error.

6. Conclusion

In this article, a stiffness identification method of MSFW rotor based on the synchronous displacements and currents of unbalance vibration is proposed. The unbalance vibration model of MSFW rotor is established, and the relationship among the stiffness coefficient, the synchronous displacement and the synchronous current is derived. Furthermore, the zero-displacement model is successfully designed to acquire the synchronous currents of MSFW system at different rotational speeds, and the zero-current model is used to pick up the synchronous displacements of MSFW rotor. Moreover, the synchronous displacements and currents could be extracted from the dynamic displacements and currents of MSFW rotor at different rotational speeds. The current stiffness and the displacement stiffness could be determined by substituting the synchronous displacements and currents into the unbalance vibration equation. The stiffness estimation error is limited to 1% from speed 3000 rpm to 5000 rpm, but the estimation precision could be declined at high rotational speed because of the nonlinearity caused by large displacement deflection of the rotor. Therefore, the proposed stiffness identification method based on the synchronous displacements and currents could be used for the determination of displacement stiffness and the current stiffness of MSFW system, but the identification accuracy would be affected by the unbalance vibration of MSFW system with great mass running at high speed.

Acknowledgement

The authors would like to thank The Hong Kong Polytechnic University of Hong Kong for the support of this research (ref: 16900506R).

Conflict of Interest Statement

The authors declare no conflict of interest in preparing this article.

References

[1] B. Xiang, W.o. Wong, Stable control of magnetically suspended motor with heavy self-weight and great moment of inertia, ISA Transactions, 105 (2020) 335-348.

[2] G. Borquegallego, L. Rossini, T. Achtnich, D.M. Araujo, Y. Perriard, Efficiency Optimisation of Slotless Magnetic Bearing Machines, IEEE Transactions on Industry Applications, (2021).

[3] A. Sahinkaya, J.T. Sawicki, Computationally efficient implementation of robust controllers in active magnetic bearing systems, Mechanical Systems and Signal Processing, 144 (2020) 106902.

[4] B. Xiang, W. Wong, Decoupling control of magnetically suspended motor rotor with heavy self-weight and great moment of inertia based on internal model control, Journal of Vibration and Control, (2021) 1077546321997611.

[5] P. Cui, J. Cui, Harmonic current suppression of active-passive magnetically suspended control moment gyro based on variable-step-size FBLMS, Journal of Vibration and Control, 23 (2017) 1221-1230.

[6] N. Nevaranta, P. Jaatinen, J. Vuojolainen, T. Sillanpää, O. Pyrhönen, Adaptive MIMO pole placement control for commissioning of a rotor system with active magnetic bearings, Mechatronics, 65 (2020) 102313.

[7] N.R. Hemenway, H. Gjemdal, E.L. Severson, New Three-Pole Combined Radial-Axial Magnetic Bearing for Industrial Bearingless Motor Systems, IEEE Transactions on Industry Applications, (2021).

[8] Y. Li, L. Zheng, Y. Liang, Y. Yu, Adaptive compensation control of an electromagnetic active suspension system based on nonlinear characteristics of the linear motor, Journal of Vibration and Control, 26 (2020) 1873-1885.

[9] B. Han, Q. Xu, Q. Yuan, Multiobjective optimization of a combined radial-axial magnetic bearing for magnetically suspended compressor, IEEE Transactions on Industrial Electronics, 63 (2016) 2284-2293.

[10] J. Asama, D. Kanehara, T. Oiwa, A. Chiba, Development of a compact centrifugal pump with a two-axis actively positioned consequent-pole bearingless motor, IEEE Transactions on Industry Applications, 50 (2014) 288-295.

[11] T. Masuzawa, S. Ezoe, T. Kato, Y. Okada, Magnetically suspended centrifugal blood pump with an axially levitated motor, Artificial organs, 27 (2003) 631-638.

[12] K. Wang, X. Ma, Q. Liu, S. Chen, X. Liu, Multiphysics Global Design and Experiment of the Electric Machine With a Flexible Rotor Supported by Active Magnetic Bearing, IEEE/ASME Transactions on Mechatronics, 24 (2019) 820-831.

[13] M.O.T. Cole, W. Fakkaew, An Active Magnetic Bearing for Thin-Walled Rotors: Vibrational Dynamics and Stabilizing Control, IEEE/ASME Transactions on Mechatronics, 23 (2018) 2859-2869.

[14] T. Wen, B. Xiang, The airborne inertially stabilized platform suspend by an axial-radial integrated active magnetic actuator system, Journal of Advanced Research, 31 (2021) 191-205.

[15] R. Zhu, W. Xu, C. Ye, J. Zhu, G. Lei, X. Li, Design Optimization of a Novel Heteropolar Radial Hybrid Magnetic Bearing Using Magnetic Circuit Model, IEEE Transactions on Magnetics, 54 (2018) 1-5.

[16] R. Safaeian, H. Heydari, Optimal design of a compact passive magnetic bearing based on dynamic modelling, in: IET Electric Power Applications, Institution of Engineering and Technology, 2019, pp. 720-729.

[17] T. Matsuzaki, M. Takemoto, S. Ogasawara, S. Ota, K. Oi, D. Matsuhashi, Novel Structure of Three-Axis Active-Control-Type Magnetic Bearing for Reducing Rotor Iron Loss, IEEE Transactions on Magnetics, 52 (2016) 1-4.

[18] F. Marignetti, M. AlizadehTir, S.M. Mirimani, An axial passive magnetic bearing using three PM rings, IET Electric Power Applications, 15 (2021) 415-428.

[19] A. Noshadi, J. Shi, W.S. Lee, P. Shi, A. Kalam, System Identification and Robust Control of Multi-Input Multi-Output Active Magnetic Bearing Systems, IEEE Transactions on Control Systems Technology, 24 (2016)

1227-1239.

[20] Y. Xu, J. Zhou, L. Di, C. Zhao, Active magnetic bearings dynamic parameters identification from experimental rotor unbalance response, Mechanical Systems and Signal Processing, 83 (2017) 228-240.

[21] J.J. Janse van Rensburg, G. van Schoor, P.A. van Vuuren, A. Janse van Rensburg, Non-linear model of rotor delevitation in an active magnetic bearing system including parameter estimation, Measurement, 109 (2017) 256-267.

[22] S.-J. Kim, C.-W. Lee, On-line identification of current and position stiffnesses by LMS algorithm in active magnetic bearing system equipped with force transducers, Mechanical Systems and Signal Processing, 13 (1999) 681-690.

[23] R. Tiwari, A. Chougale, Identification of bearing dynamic parameters and unbalance states in a flexible rotor system fully levitated on active magnetic bearings, Mechatronics, 24 (2014) 274-286.